

## Sub-millimetre accurate human hand kinematics: from surface to skeleton

Jumana Ma'touq, Tingli Hu & Sami Haddadin

To cite this article: Jumana Ma'touq, Tingli Hu & Sami Haddadin (2018) Sub-millimetre accurate human hand kinematics: from surface to skeleton, *Computer Methods in Biomechanics and Biomedical Engineering*, 21:2, 113-128, DOI: [10.1080/10255842.2018.1425996](https://doi.org/10.1080/10255842.2018.1425996)

To link to this article: <https://doi.org/10.1080/10255842.2018.1425996>



© 2018 The Author(s). Published by Informa UK Limited, trading as Taylor & Francis Group.



[View supplementary material](#)



Published online: 27 Jan 2018.



[Submit your article to this journal](#)



Article views: 172



[View Crossmark data](#)

## Sub-millimetre accurate human hand kinematics: from surface to skeleton

Jumana Ma'touq<sup>a</sup>, Tingli Hu<sup>a</sup> and Sami Haddadin<sup>a,b</sup>

<sup>a</sup>Institute of Automatic Control, Leibniz Universität Hannover, Hannover, Germany; <sup>b</sup>Center for Systems Neuroscience, Hannover, Germany

### ABSTRACT

A highly accurate human hand kinematics model and identification are proposed. The model includes the five digits and the palm arc based on mapping function between surface landmarks and estimated joint centres of rotation. Model identification was experimentally performed using a motion tracking system. The evaluation of the marker position estimation error, which is on sub-millimetre level across all digits, underlines model quality and accuracy. Noticeably, with the development of this model, we were able to improve various modelling assumptions from literature and found a basic linear relationship between surface and skeleton rotational angles.

### ARTICLE HISTORY

Received 3 July 2017  
Accepted 7 January 2018

### KEYWORDS

Hand kinematics; joint centre of rotation; hand motion analysis; hand biomechanics; thumb biomechanics

### 1. Introduction

The analysis and evaluation of human hand kinematics is essential for developing human-like smart prostheses and articulated robotic hands. The kinematic complexity of the human hand makes accurate modelling a challenging task. Despite that tremendous progress has been made, a complete and accurate kinematics model with its corresponding identification procedure is still lacking. In fact, limitations are still present in the state of the art as follows.

- (1) Specific types of isolated joints such as metacarpophalangeal (MCP) (Speirs et al. 2001) or 2nd–5th digits (Braido and Zhang 2004) or specific digits (Parasuraman and Zhen 2009; Nataraj and Li 2013; Nataraj and Li 2015) were considered. More extended models with varying modelling assumptions and accuracy were also developed, see Table 1.
- (2) The thumb has been modelled with different assumptions regarding its number of degrees of freedom (DoFs). The state-of-the-art thumb models include 4 DoFs (Cerveri et al. 2007; Metcalf et al. 2008; Cobos et al. 2010) and 5 DoFs (Miyata et al. 2004; Veber and Bajd 2006; Parasuraman and Zhen 2009; Cordella et al. 2014; Peña Pitarch et al. 2014), see Table 1. Yet, a highly accurate thumb model is still lacking. Moreover, some thumb models did not relate it to its own reference system (Carpinella et al. 2006; Veber and Bajd 2006; Cordella et al. 2014). In fact, thumb


movements in the plane of the hand may occur as a result of combined joint movements (Kuczynski 1974). Thus, a separate coordinate system is required to describe motions at the trapeziometacarpal (TM) joint (Cooney et al. 1981).

- (3) Finger joint centres of rotation (CoRs) cannot be simply substituted by surface landmark positions (Supuk et al. 2004) and estimation of CoRs is important in describing the skeletal kinematics (Zhang et al. 2003). Available CoR estimation includes simple translation (Cerveri et al. 2007), optimisation routines (Zhang et al. 2003; Supuk et al. 2004), and optimisation with circle intersection (Miyata et al. 2004; Veber and Bajd 2006). However, no forward and inverse functions between surface landmarks and CoRs were proposed in the aforementioned works. Furthermore, thumb joint CoRs have not been identified yet.
- (4) The need for specially designed experimental setups (Degeorges et al. 2005; Shen et al. 2012; Nataraj and Li 2013).

*Contribution.* This paper aims to provide and validate a highly accurate human hand kinematics model. Specifically, our contributions are as follows.

- (1) Developing a complete accurate hand model, including the four fingers (4 DoFs each), the thumb (6 DoFs) and the palm arc (4 DoFs), see Table 1.
- (2) Designing a highly accurate thumb kinematics model associated to its own frame of reference, which is identified in subject-specific relationships

**CONTACT** Jumana Ma'touq  [matouq@irt.uni-hannover.de](mailto:matouq@irt.uni-hannover.de), [j\\_matouq@yahoo.com](mailto:j_matouq@yahoo.com)

 Supplemental data for this article can be accessed at <https://doi.org/10.1080/10255842.2018.1425996>

© 2018 The Author(s). Published by Informa UK Limited, trading as Taylor & Francis Group.

This is an Open Access article distributed under the terms of the Creative Commons Attribution-NonCommercial-NoDerivatives License (<http://creativecommons.org/licenses/by-nc-nd/4.0/>), which permits non-commercial re-use, distribution, and reproduction in any medium, provided the original work is properly cited, and is not altered, transformed, or built upon in any way.

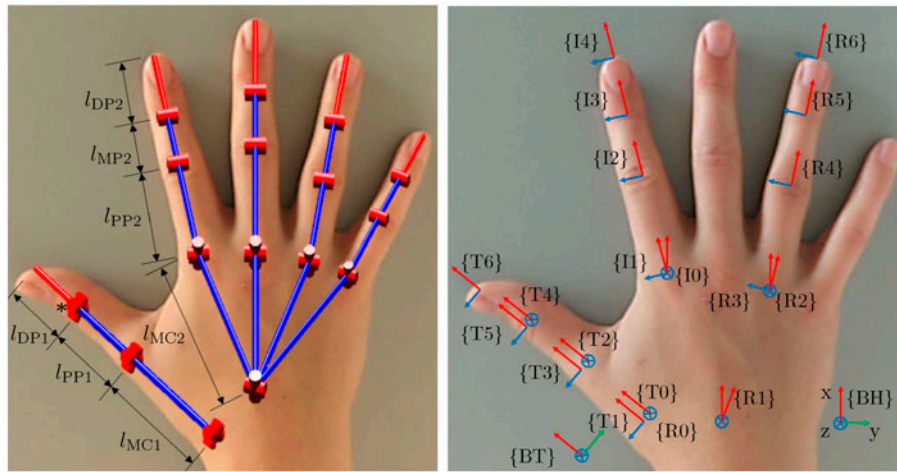


**Figure 1.** The proposed human hand kinematics model with 26 DoFs. Left: representation of the serial linkages for each digit, which is assumed to be a rigid body segment. The 2nd–5th digits have 4 DoFs (2 DoFs for MCP joint F/E and Ab/Ad and 2 DoFs for PIP and DIP joints F/E), while the 1st digit has 6 DoFs (2 DoFs for F/E and Ab/Ad for each joint). In the thumb model, the Ab/Ad of the IP joint is considered passive (indicated by ‘\*’) while the other 5 DoFs are actuated. The palm arc is modelled as Ab/Ad and F/E of the two palm joints. Right: coordinate systems for each digit and the hand base. The alphabet in the CS naming indicates the digit initial.

to the hand dorsal reference frame. Based on an in-depth literature review, this is to the authors’ knowledge the first study investigating such relationships using a motion tracking technique.

- (3) Highlighting the effect of considering passive DoF on the kinematics model accuracy, i.e. additional passive DoF in the thumb. This formalises a first hint towards joint flexibility.
- (4) Proposing a systematic flexion/extension CoR estimation algorithm and the forward and inverse kinematics mapping between surface and skeleton kinematics.
- (5) Proposing a practical identification procedure for standard motion tracking techniques.

## 2. Methods

### 2.1. Hand biomechanics and modelling assumptions

A human hand is composed of five digits and the palm. The 2nd–5th digits have three joints with 4 DoFs of MCP flexion/extension (F/E) and abduction/adduction (Ab/Ad), proximal interphalangeal (PIP) F/E, and distal interphalangeal (DIP) F/E (Lippert 2011). Thumb and palm arc biomechanics and modelling assumptions are discussed as in the following.

**Thumb.** The thumb has three joints with more complex DoFs. The carpometacarpal (CMC) (or TM joint) has 2 DoFs (F/E and Ab/Ad) and permits some axial rotation (Lippert 2011). The MCP joint has 2 DoFs (Kapandji 2007) and might be modelled as 1 DoF (Cobos et al. 2010).

In our pilot experiments, we found that the thumb has significant passive DoF (elastic behaviour which might originate from joint capsule elasticity) which occur in interphalangeal (IP) joint during physical interactions between objects and thumb. Such interactions result in thumb distal phalange pronation, which is modelled by 1 passive DoF (Ab/Ad) in the IP joint. Thus, the proposed thumb model has 6 DoFs (1 passive<sup>1</sup> and 5 actuated<sup>2</sup> DoFs). To show the importance of the additional 1 passive DoF and the accuracy of the proposed 6 DoFs thumb model in comparison with the state-of-the-art thumb models, the following three models are compared and discussed (Section 3.2):

- 4 DoF thumb model (4 actuated DoFs, without passive DoFs),
- 5 DoF thumb model (5 actuated DoFs, without passive DoFs),
- 6 DoF thumb model (5 actuated DoFs, with 1 passive DoF).

**Palm arc.** The overall function of the CMC joints and their segments is to contribute to the palm arc system (Levangie and Norkin 2005). The precise positions of the four CMC joints are difficult to estimate from motion because of their very small range of movement (Miyata et al. 2004) where the 4th–5th CMC joints rotate with F/E and Ab/Ad and the 2nd–3rd CMC are static (Peña Pitarch et al. 2005). Therefore, the formed palm arc is modelled as two *palm joints*, with each one having 2 DoFs. In order to highlight the importance of considering palm arc on the accuracy of hand kinematics modelling, more specifically on pinky finger pose estimation, two models of the 2nd

**Table 1.** State-of-the-art hand kinematics models.

Model	DoFs			Error	CoR identification
	1st	2nd–5th	Palm arc		
Miyata et al. (2004)	5 <sup>a</sup>	5	✓	Up to 2.98 mm	✓
Veber and Bajd (2006)	5	4	×	n.a.	✓
Cerveri et al. (2007)	4	4	×	Up to 3.25 mm	✓ <sup>b</sup>
Carpinella et al. (2006)	3	2	×	n.a.	×
Metcalf et al. (2008)	4	4	✓	n.a.	×
Cordella et al. (2014)	5	4	×	Up to 10.67 mm	×
Cobos et al. (2010)	4	4 <sup>c</sup>	✓	n.a.	×
Parasuraman and Zhen (2009)	5	4 <sup>d</sup>	×	n.a.	×
Peña Pitarch et al. (2014)	5	4 <sup>e</sup>	✓	n.a.	×
Proposed model	6	4	✓	Sub-millimetre	✓

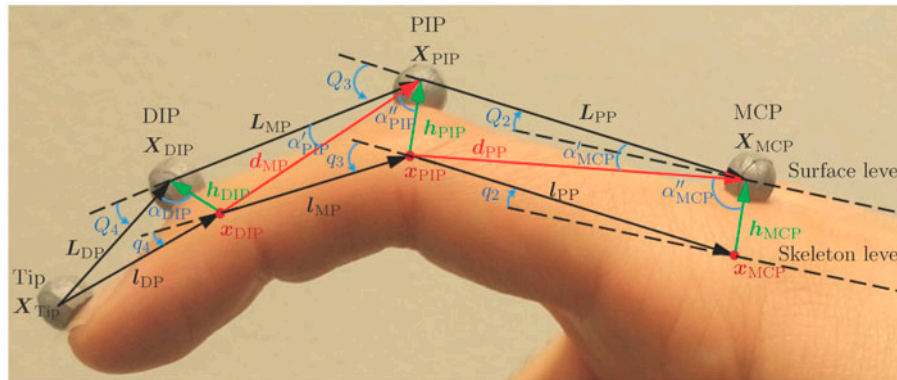
<sup>a</sup>Although '8 DoFs' is mentioned explicitly in Miyata et al. (2004), but 3 of them are the translation from {BH} to {BT}. Due to that, we consider it as a 5 DoF model.

<sup>b</sup>CoR estimation includes simple translation.

<sup>c</sup>The CMC1–CMC4 DoFs are considered here in palm arc DoFs.

<sup>d</sup>Middle and ring fingers only.

<sup>e</sup>The CMC4 and CMC5 DoFs are considered here in palm arc DoFs.

**Figure 2.** Two-dimensional finger schematic diagram.

Notes: The surface link vector  $L_{\square}$  changes its length during F/E whereas that of a skeletal link vector  $l_{\square}$  is constant. Bone lengths,  $l_{\square} = \|l_{\square}\|$ , are calculated from the anthropometric model of Buchholz et al. (1992).

palm joint are compared and discussed (Section 3.1). The compared models have the following characteristics:

- Two DoFs where the palm arc is modelled,
- A static joint where the palm arc is not modelled.

In summary, the proposed model has 26 DoFs, of which 4 DoFs describe each of 2nd–5th digits, 4 DoFs describe the palm arc and 6 DoFs (5 actuated and 1 passive DoF) describe the thumb, see Figure 1.

## 2.2. Surface and skeletal kinematics model

The proposed model connects two representation levels, namely the *skeletal level* and the *surface level*, see Figure 2. These correspond to *centres of rotation* and *skin landmarks*, respectively. For obvious reasons, it is chosen to be the *skeletal joint position vector*  $\mathbf{q} := [q_1 \dots q_{26}]^T \in \mathbb{R}^{26}$  and the set of surface Cartesian positions  $\{\mathbf{X}_i\}$ . Furthermore, the two auxiliary coordinates *surface joint configuration*  $\mathbf{Q} := [Q_1 \dots Q_{26}]^T \in \mathbb{R}^{26}$  and the set of joint

*CoR positions*  $\{\mathbf{x}_i\}$  are introduced. The desired mapping  $\{\mathbf{X}_i\} \rightarrow \mathbf{q}$  is divided into composable sub-mappings. Overall two different types of mappings are categorised as follows.

(1) Intra-level mappings:

- CoR positions and skeletal joint positions:  $\{\mathbf{x}_i\} \leftrightarrow \mathbf{q}$
- Surface landmark positions and surface joint positions:  $\{\mathbf{X}_i\} \leftrightarrow \mathbf{Q}$

(2) Inter-level mapping: denoting the transition between surface level and skeletal level representations

### 2.2.1. Intra-level mapping

*Surface Kinematics.* Surface kinematics describe the relationship between the skin landmark Cartesian positions  $\mathbf{X}_i \in \mathbb{R}^3$  and the *surface joint configuration*  $\mathbf{Q} \in \mathbb{R}^{26}$ :

$$\mathbf{X} := (\mathbf{X}_1 \mathbf{X}_2 \dots \mathbf{X}_i \dots \mathbf{X}_{25})^T, \quad (1a)$$



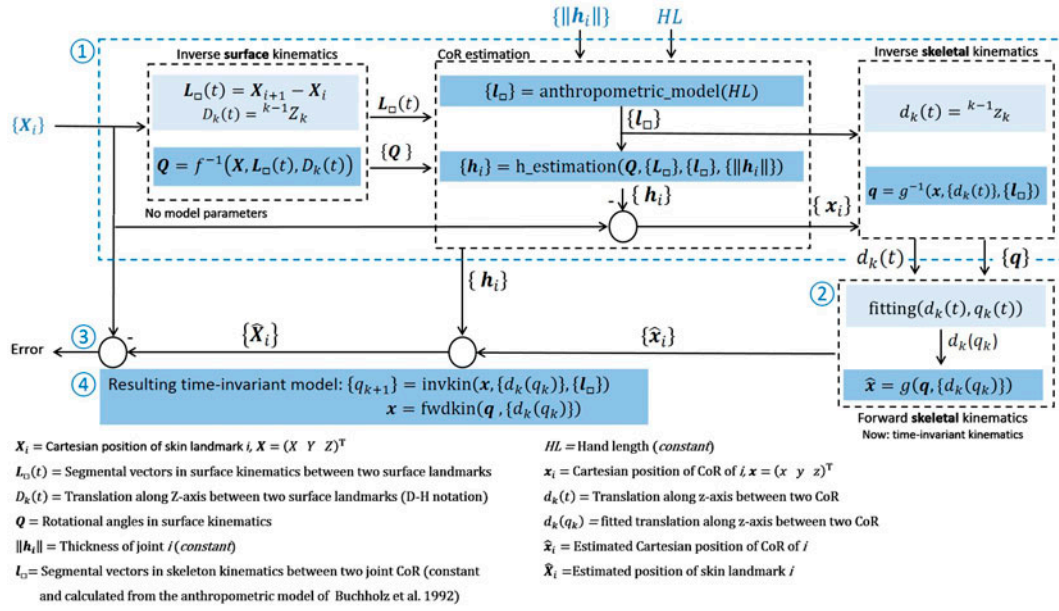


Figure 3. Block diagram of model identification and validation.

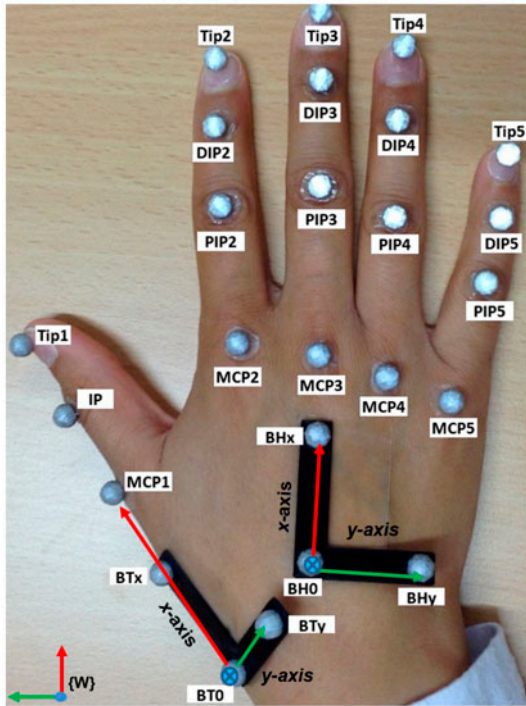


Figure 4. Maker placement and labelling.

Notes: In the five digits, markers were attached to the heads of metacarpals and of phalanges. Markers were labelled to indicate the joint names and the digit numbers (1: thumb, . . . , 5: pinky). Two reference clusters, BH (BHx-BH0-BHy) and BT (BTx-BT0-BTy), were used to establish reference coordinates. Cluster BH is used to track {BH} and represents its floating reference. Cluster BT is fixed on the base of the first metacarpal bone to identify the thumb reference plane.

$$\mathbf{Q} := (Q_1 \ Q_2 \ \cdots \ Q_k \ \cdots \ Q_{26})^T, \quad (1b)$$

$$\mathbf{X} = f(\mathbf{Q}), \quad (1c)$$

$$\mathbf{Q} = f^{-1}(\mathbf{X}), \quad (1d)$$

where  $f(\cdot)$  and  $f^{-1}(\cdot)$  denote the forward and inverse surface kinematics, respectively. In order to find  $f(\cdot)$  and  $f^{-1}(\cdot)$ , two base frames and one frame for each joint DoF are established, see Figure 1. These base frames are the *Hand Base frame* {BH} and the *Thumb Base frame* {BT}, which are related to each other via:

$${}^{\text{BH}}T_{\text{BT}} = \begin{pmatrix} {}^{\text{BH}}R_{\text{BT}} & {}^{\text{BH}}X_{\text{BT0}} \\ \mathbf{0}^T & 1 \end{pmatrix}, \quad (2)$$

where  ${}^{\text{BH}}R_{\text{BT}} \in \mathbb{R}^{3 \times 3}$  denotes the rotation matrix.  ${}^{\text{BH}}X_{\text{BT0}} \in \mathbb{R}^{3 \times 1}$  denotes the vector pointing from the origin of {BH} to the origin of {BT}, represented by BT0. Joint DoF frames are determined by transforming from the base frames via

$$\begin{pmatrix} {}^kX_i \\ 1 \end{pmatrix} = {}^kT_{\text{B}}(\mathbf{Q}_k) \begin{pmatrix} {}^{\text{B}}X_i \\ 1 \end{pmatrix} \quad (3)$$

together with the classical Denavit–Hartenberg (D–H) convention (Reddy 2014). The D–H parameters are listed in Table A1. Then, homogeneous transformation matrices  ${}^kT_{\text{B}} \in \mathbb{SE}(3)$  can be formulated as a function of  $\mathbf{Q}_k := (Q_1 \ Q_2 \ \cdots \ Q_k)^T$ . Equation (3) can be solved for  $\mathbf{Q}_k$  by using the property  ${}^kX_i = (0 \ 0 \ 0)^T$ , i.e. being the origin of frame  $k$ , and by assuming  ${}^{\text{B}}X_i \in \mathbb{R}^3$  to be known, see Appendix 2.

*Skeletal kinematics.* The skeletal kinematics connects Cartesian positions of joint CoR  $\mathbf{x}_i \in \mathbb{R}^3$  with the *skeletal*

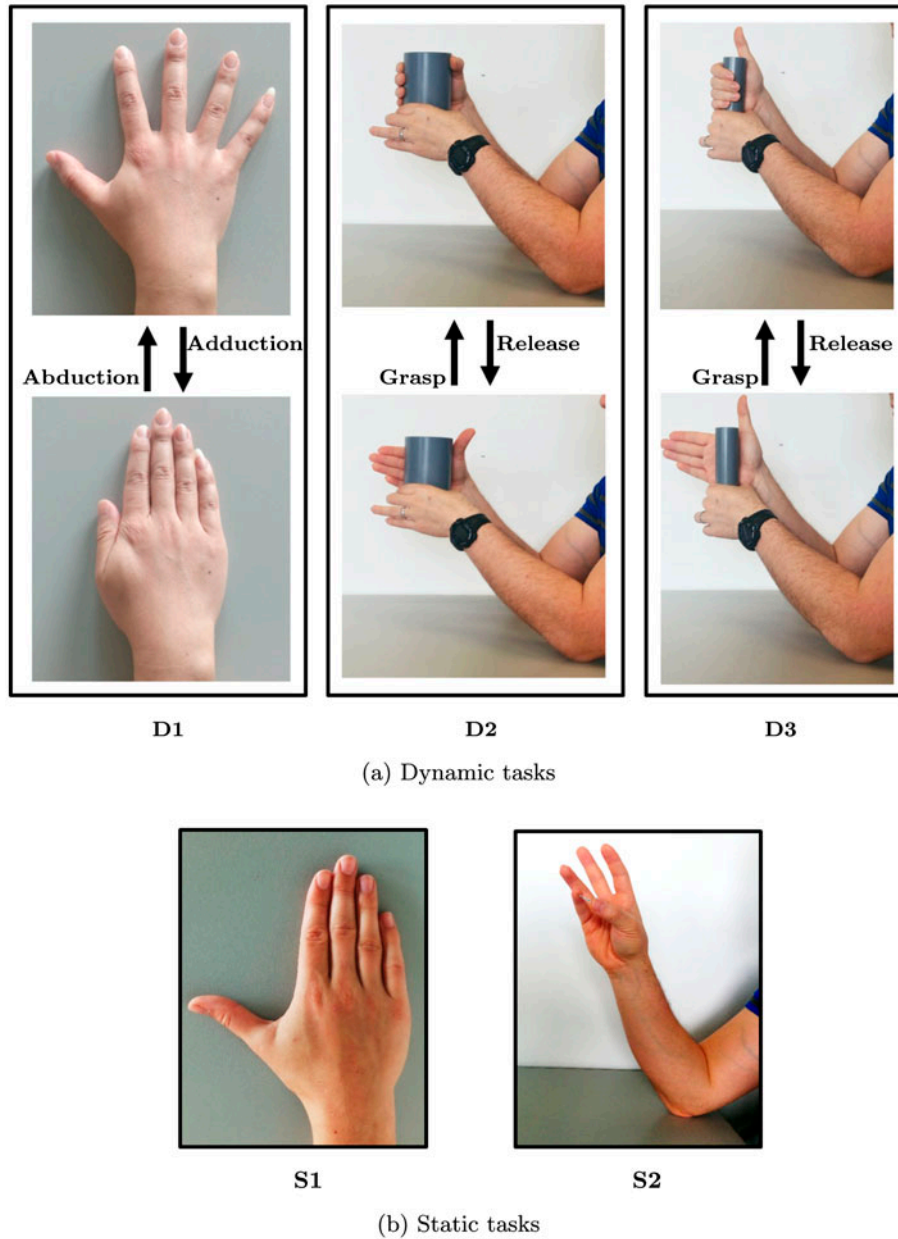


**Figure 5.** Experimental tasks.

Notes: Dynamic tasks: D1: MCP joints Ab/Ad, D2: grasp/release a cylinder with diameter of 80 mm, D3: grasp/release a cylinder with diameter of 40 mm. Static tasks: S1: static relaxed reference posture with all joints extended, S2: grasping a small paper clip by thumb and pinky digits (thumb-pinky opposition).

joint configuration  $\mathbf{q} \in \mathbb{R}^{26}$ , i.e.

$$\mathbf{x} := (\mathbf{x}_1 \ \mathbf{x}_2 \ \cdots \ \mathbf{x}_i \ \cdots \ \mathbf{x}_{15})^\top, \quad (4a)$$

$$\mathbf{q} := (q_1 \ q_2 \ \cdots \ q_k \ \cdots \ q_{26})^\top, \quad (4b)$$

$$\mathbf{x} = g(\mathbf{q}), \quad (4c)$$

$$\mathbf{q} = g^{-1}(\mathbf{x}), \quad (4d)$$

where  $g(\cdot)$  and  $g^{-1}(\cdot)$  are the skeletal forward and inverse kinematics, respectively. In order to find them, similarly to the surface kinematics, a set of reference frames is

established; however, with a different D–H parameter set, see Table A2. Analogous to the surface kinematics, the homogeneous transformation matrix  ${}^k t_B \in \mathbb{SE}(3)$  is a function of  $\mathbf{q}_k := (q_1 \ q_2 \ \cdots \ q_k)^\top$ , and (5) can be solved for  $\mathbf{q}_k$  by knowing  ${}^k \mathbf{x}_i = (0 \ 0 \ 0)^\top$  as the origin of frame  $k$ , and  ${}^B \mathbf{x}_i$  from inter-level mapping (Section 2.2.2).

$$\begin{pmatrix} {}^k \mathbf{x}_i \\ 1 \end{pmatrix} = {}^k t_B(\mathbf{q}_k) \begin{pmatrix} {}^B \mathbf{x}_i \\ 1 \end{pmatrix}. \quad (5)$$

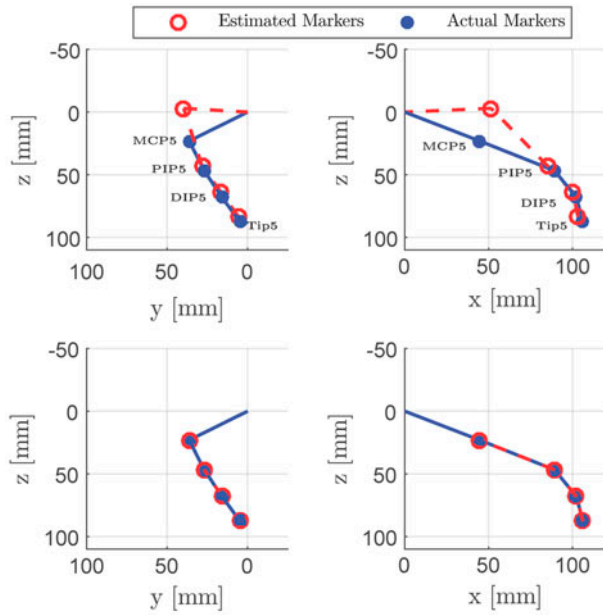


**Figure 6.** Comparison between measured and estimated  $X_i$  in two models of the 2nd palm joint. Top: static joint model (without considering palm arc). Bottom: 2 DoF joint model (with considering palm arc). The figure shows the pinky finger of an exemplar subject expressed in {BH}.

### 2.2.2. Inter-level mapping

In the previous section surface and skeletal kinematics were introduced. The mapping between these two levels is done by the inter-level mapping. Figure 2 depicts surface and skeletal level positions, which are related to each other by the vectors  $h_i$  as

$$X_i = x_i + h_i. \quad (6)$$

The estimation of  $h_i$  is performed in 2-D space to minimise the number of unknowns (Zhang et al. 2003). For the 2nd–5th digits, the best frame for 2-D projection is MCP F/E frame, defined as {1}, where F/E occurs and one moves with Ab/Ad motion accordingly. The thumb has Ab/Ad DoF in each joint which make the F/E motion in different planes. Thus, the CoR of CMC is calculated in frame {T1}, while the CoR of MCP and IP joints are obtained in frames {T3} and {T5}, respectively, see Figure 1. In the 2-D spaces (Figure 2), the Law of Cosines and dot product are used to estimate  $h_i$  as explained in Appendix 3.

### 2.3. Model identification and validation

Obviously, the simultaneous measurement of motion capture data with online high frequency imaging for model validation would be ideal for validation. However, since this is technically not feasible, especially for high-

frequency motions, our algorithm is evaluated according to the consistency scheme shown in Figure 3. The model self-consistency and accuracy are evaluated as follows: in the inverse calculation path, only measurements  $\{X_i\}$ ,  $\{\|h_i\|\}$ , and  $HL$  serve as the input to estimate the skeletal joint position  $q$ , whereas in the forward calculation path,  $q$  and the calibrated kinematics model with fitted model relation  $\{d_k(q_k)\}$  are required to estimate  $\{\hat{X}_i\}$ . The difference between  $\{X_i\}$  and  $\{\hat{X}_i\}$  quantifies model consistency and accuracy. The practical identification procedure was performed as follows.

#### 2.3.1. Algorithmic identification procedure

In the proposed model, two floating base coordinate systems are used: {BH} and {BT}, see Figure 4. The identification of {BH} is performed at every time step, while {BT} is established by defining a rotation matrix between {BH} and {BT} in the reference posture as explained in Appendix 4. Thereafter, the overall identification procedure that estimates the joint angles  $q$  from measured marker positions  $X_i$  is performed, see Appendix 4.

#### 2.3.2. Experimental setup

Nine healthy subjects (7 males and 2 females, age =  $29.11 \pm 4.20$  years with hand length ( $HL$ ) =  $183.83 \pm 8.35$  mm) volunteered for this study. All participants provided written consent prior to their participation. The test procedures were conducted according to the guidelines of the *Declaration of Helsinki* and approved by the ethics committee of *Leibniz Universität Hannover, Germany*.

Twenty-five reflective spherical markers were attached on specific bony landmarks, see Figure 4. In the five digits, markers were attached to the heads of metacarpals and of phalanges as suggested by Metcalf et al. (2008). In each trial, marker coordinates were acquired during two static and three dynamic tasks using an optoelectronic motion capture system (©Vicon Motion Systems Ltd., UK with its associated software Nexus 2.0), see Figure 5.

## 3. Results and discussions

The block diagram of model identification and validation is shown in Figure 3. The sub-millimetre difference between  $\{X_i\}$  and  $\{\hat{X}_i\}$  indicates that the proposed model and associated identification procedure are consistent and highly accurate. This also validates the proposed CoRs estimation algorithm, which is part of the model. The detailed results and discussions of the individual assumptions follow now.

### 3.1. Palm arc modelling

The aim of this section is to highlight the effect that modelling the palm arc has on the pose estimation

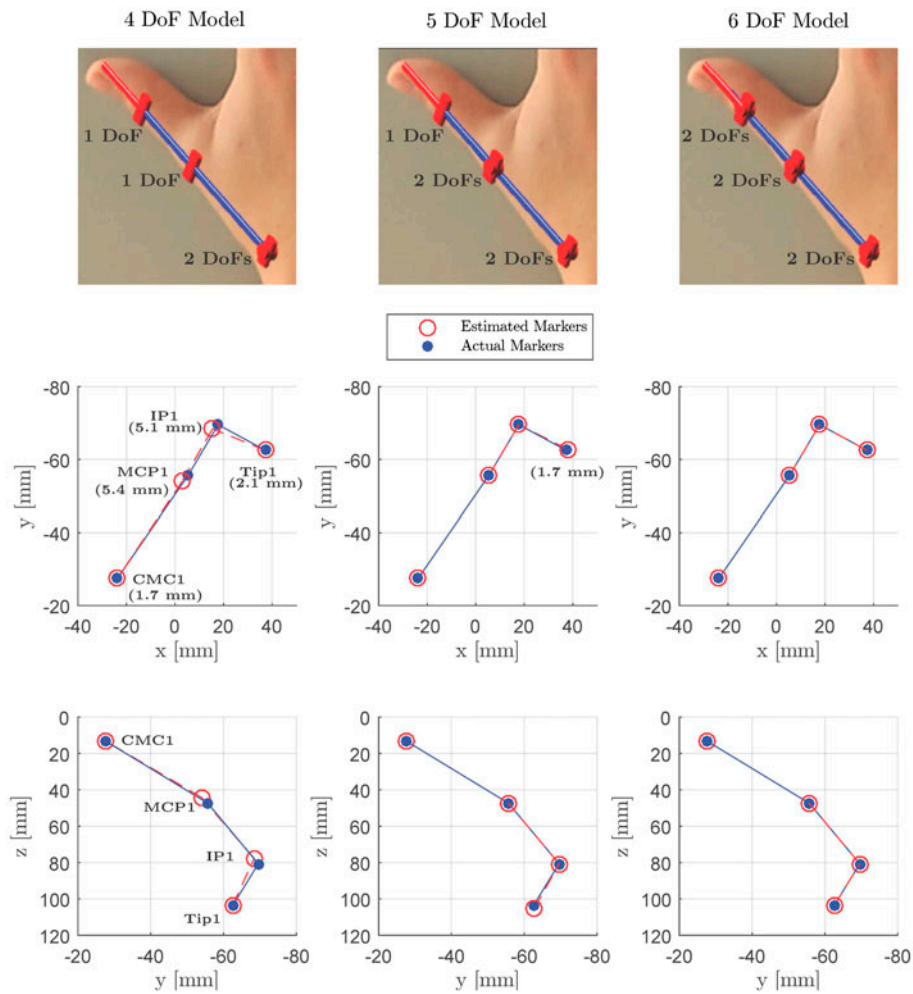


**Figure 7.** Comparison between measured and estimated  $X_i$  expressed in {BH} for 4 DoF (left), 5 DoF (middle) and 6 DoF (right) thumb models for an exemplar subject. The top row shows a representation of the serial linkage of the compared three models. The estimation error, defined as the maximal Euclidean distance between measured and estimated  $X_i$ , is represented by the numbers in brackets for the corresponding  $X_i$ .

accuracy of the pinky finger. The difference between the estimated and measured  $X_i$  during Task S2, resulted from the compared models of the 2nd palm joint, is depicted in Figure 6. In the static palm joint model, the error in terms of the Euclidean norm among different subjects is up to 65.0, 20.0, 10.6 and 9.3 mm for  $X_{MCP5}$ ,  $X_{PIP5}$ ,  $X_{DIP5}$  and  $X_{Tip5}$ , respectively. As one may notice,  $X_{MCP5}$  exhibits the largest error, especially along the z-axis of {BH} coordinate system, see Figure 6 top. This phenomenon emphasises that the static joint model estimates  $X_{MCP5}$  on the x-y plane of the {BH} (z-component close to zero), while the true position is shifted downwards to form the palm arc. In our proposed 2 DoF model, only sub-millimetre errors could be observed between estimated and measured  $X_i$ , see Figure 6 bottom.

### 3.2. Thumb modelling

In this section, thumb modelling results and considerations are discussed as follows.

*Rotational relationship between {BT} and {BH}.* The identification of  ${}^{BH}R_{BT}$  is shown in Algorithm 1. A difference ranging between  $10.6^\circ$  and  $24.3^\circ$  was noticed in  ${}^{BH}R_{BT}$  among subjects which is probably caused by the variation in population and marker placement. Conclusively, it would be more accurate to identify  ${}^{BH}R_{BT}$  for each subject rather than using fixed values. This identification results in an adaptable model which minimises the effect of individual variations.

*Thumb model DoFs and accuracy.* The difference between the estimated and measured  $X_i$  in the compared



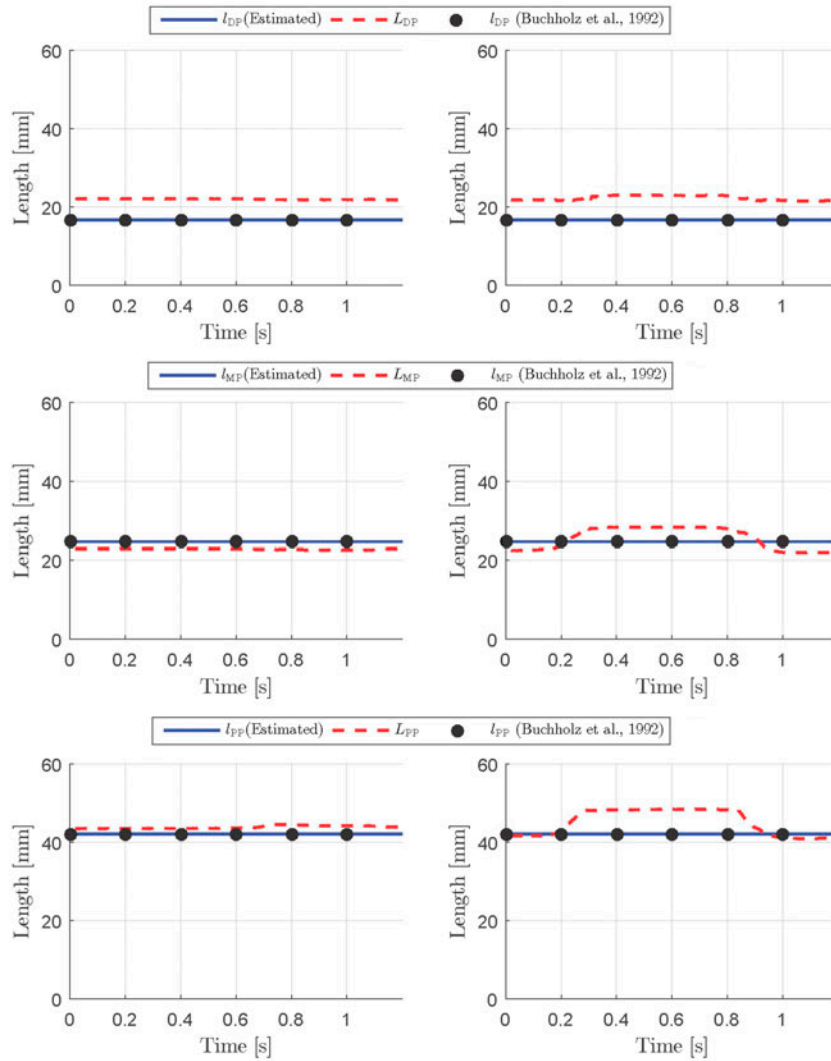


**Figure 8.** Comparison between  $\|L_{\square}\|$  and the estimated  $\|I_{\square}\|$  in Tasks D1 (left) and D2 (right). This figure shows segment lengths of an exemplar index finger. Segment lengths are compared to anthropometrically modelled segment lengths (Buchholz et al. 1992).

three thumb models is shown in Figure 7. From there, it becomes clear that the insufficient number of DoFs affects the accuracy of the model. In the 4 DoF model an error is observed in all  $X_i$  due to not considering the Ab/Ad of MCP1 and IP joints. Compared to the 4 DoF model, the 5 DoF model shows improved accuracy in all  $X_i$ , nearly to almost negligible error except in  $X_{\text{Tip1}}$ . This is due to the absence of IP Ab/Ad DoF. Despite that the IP joint has been modelled as single DoF in the available thumb models (Miyata et al. 2004; Cerveri et al. 2007; Metcalf et al. 2008; Parasuraman and Zhen 2009; Cobos et al. 2010; Cordella et al. 2014), considering the Ab/Ad is of vital importance to reconstruct tip positions accurately. In our pilot experiment, a combination of F/E and Ab/Ad at IP joint was observed, especially

during physical interactions between the thumb segments and the grasped object, where the DP of thumb rolls over the object's surface to achieve a stable grasp. This phenomenon might be related to elastic joint capsules. Besides, there are non-constant bone segment lengths being reconstructed by 4 DoF and 5 DoF models. To tackle these issues, a 6 DoF model is proposed which includes 5 active DoFs and 1 passive DoF. The proposed thumb model has an improved accuracy in all  $X_i$  compared to the other two models (4 DoF and 5 DoF models), see Figure 7. Compared to the literature models (Table 2) our proposed 6 DoF model has proved to provide significantly better accuracy with no difference was noticed between measured and estimated  $X_i$ .

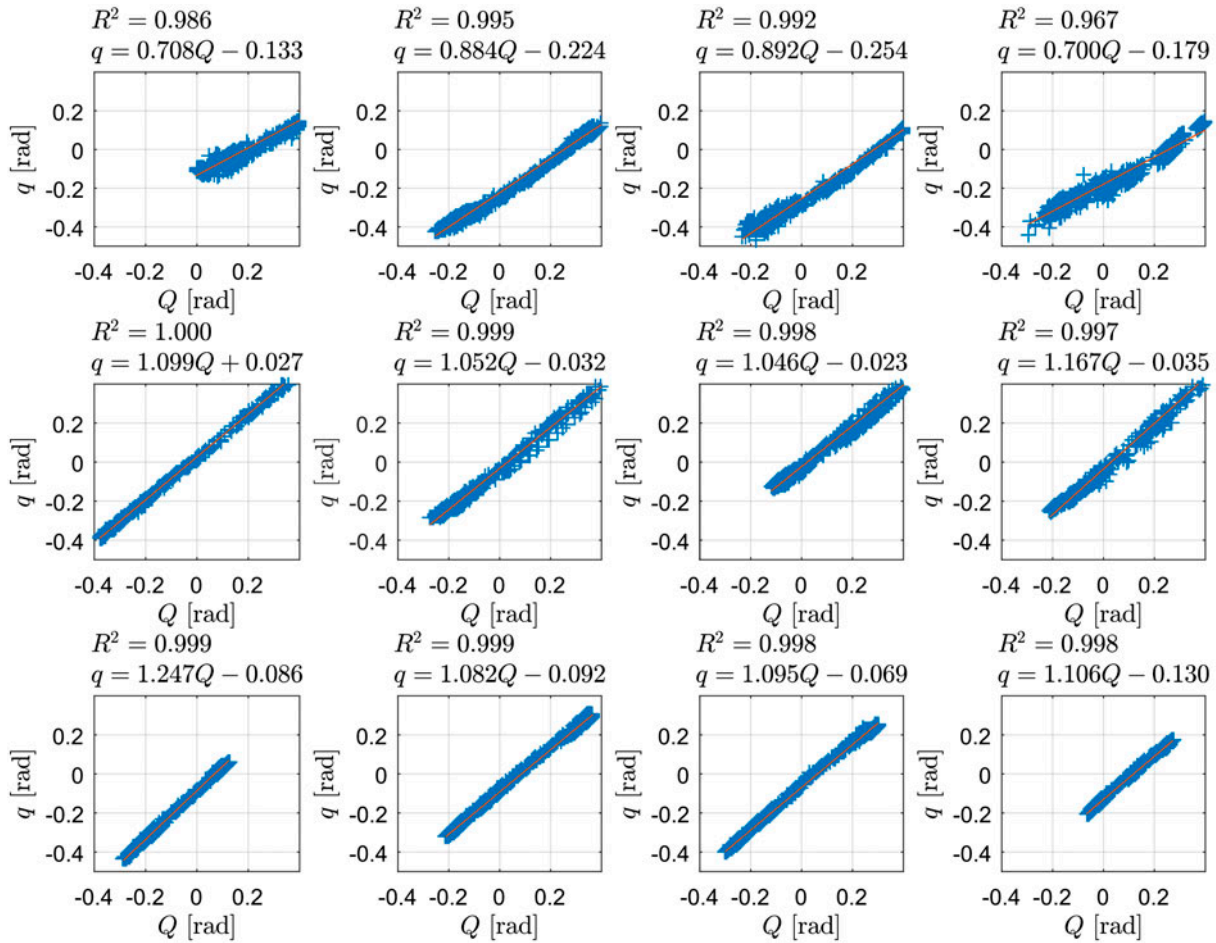


**Figure 9.** Skeleton rotational angles  $q_k$  with respect to surface rotational angles  $Q_k$  in Task D2. Columns indicate fingers (left to right): index, middle, ring and pinky. Rows indicate rotational angles (top to bottom): DIP F/E, PIP F/E and MCP F/E. For MCP Ab/Ad, the rotational rotation angles on surface level and skeleton level are equal with  $R^2 = 1.000$ , thus they are not shown in this figure.

**Table 2.** Comparison of accuracy among different models from literature.

Model	1st digit			
	$E_{TM}$ [mm]	$E_{MCP1}$ [mm]	$E_{IP}$ [mm]	$E_{Tip1}$ [mm]
Miyata et al. (2004)	n.a.	n.a.	n.a.	2.00
Cordella et al. (2014)	n.a.	0	0.77	4.33
Cerveri et al. (2007)	1.99–2.01	0.57–0.93	1.19–1.51	1.99–2.18
Model	2nd–5th digits			
	$E_{Index}$ [mm]	$E_{Middle}$ [mm]	$E_{Ring}$ [mm]	$E_{Pinky}$ [mm]
Miyata et al. (2004)	1.47	2.25	2.98	2.67
Cordella et al. (2014)	6.90	8.00	6.67	10.67
Cerveri et al. (2007)	0.42–1.66	n.a.	n.a.	n.a.

Notes: The error was calculated as the maximum error of fingertip (Miyata et al. 2004), maximum of the errors in  $x$ -,  $y$ -,  $z$ -directions (Cordella et al. 2014), and RMS error of the distance between estimated and measured marker positions (Cerveri et al. 2007).

### 3.3. Surface kinematics and skeleton kinematics

In this section, segment lengths, joint rotational angles and Cartesian errors are compared between surface and skeleton kinematics.

*Segment lengths.* Surface segmental length  $\|L_{\square}\|$  are different from  $\|I_{\square}\|$ , see Figure 8. This difference sup-

ports our hypothesis that surface kinematics is not the same as skeletal kinematics. Surface segmental length  $\|L_{\square}\|$  varies over time due to:

- (1) skin displacement relative to skeleton, and
- (2) rotation of markers about the DoF axes during movements.

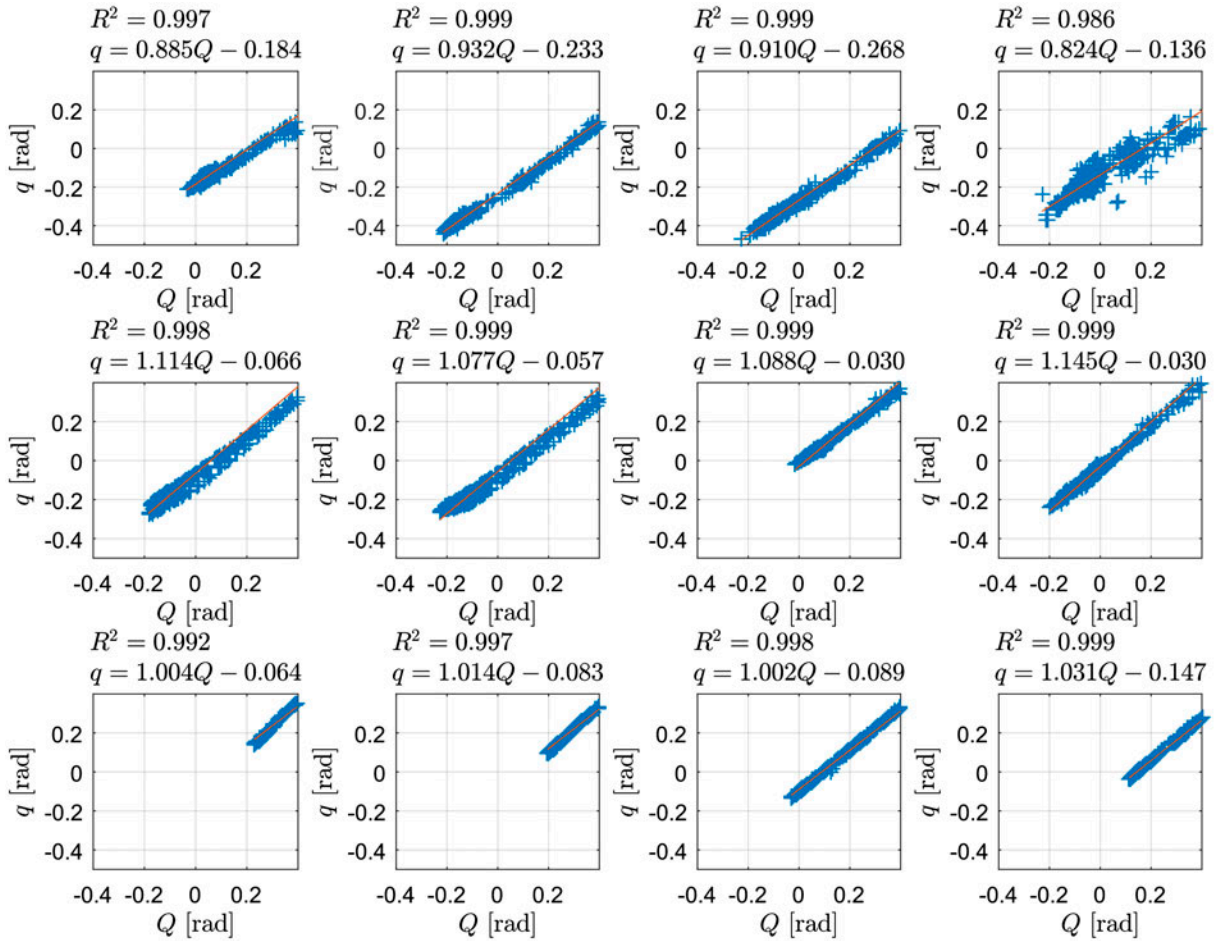


**Figure 10.** Skeleton rotational angles  $q_k$  with respect to surface rotational angles  $Q_k$  in Task D3. Columns indicate fingers (left to right): index, middle, ring and pinky. Rows indicate rotational angles (top to bottom): DIP F/E, PIP/F/E, and MCP F/E. For MCP Ab/Ad, the rotational rotation angles on surface level and skeleton level are equal with  $R^2 = 1.000$ , thus they are not shown in this figure.

Consequently,  $\|I_{\square}\|$  should be used to calculate joint angles. Compared to the anthropometrically modelled segment lengths from Buchholz et al. (1992), the proposed model lengths are equal in the four fingers, see Figure 8.

*Joint rotational angles.* The relationship between  $q_k$  and  $Q_k$  in Tasks D2 and D3 is shown in Figures 9 and 10. Experimental data revealed a highly linear relationship between F/E angles in all joints with  $R^2 \geq 0.94$  in most of joints. From the linear regression coefficients, the difference between  $q_k$  and  $Q_k$  in terms of both slopes and intercepts is clear.

*Errors in Cartesian space.* The Cartesian errors are calculated as the difference between marker positions ( $X_i$ ) estimated by the forward kinematics model and the positions directly measured by the motion capture system, see Figure 3. In surface kinematics, an error increase has been noticed along the serial chain from MCP landmark to tip of 2nd–5th digits (Cerveri et al. 2007; Cordella et al. 2014). This can be explained by finger curvature (Cordella et al. 2014), which is equivalent to

$D_k \neq 0$  and  $d_k \neq 0$  in the used D–H notation (Appendix 1). To overcome this issue, in the proposed model  $D_k$  is calculated based on the experimental measurements from motion tracking data, while  $d_k$  is fitted as a function of  $q_k$  (in our case polynomial regression), see Figure 3. This improves the model accuracy to a sub-millimetre error in most cases. Only in one case, an error of nearly 2 mm was observed due to the improper  $d_k$ – $q_k$  fitting. This, however, could be solved easily with more complex fitting algorithms. In addition, the variance of  $d_k$  during tasks should be further investigated with respect to joint DoFs, joint capsule elasticity and physical finger-object interaction in the future.

Compared to the available and comparable models in the literature (Table 2), our proposed model has proved to be highly accurate without a noticeable difference between measured and estimated  $X_i$ , see Figure 11. This sub-millimetre accuracy evidences the model self-consistency (see Figure 3) and, ergo, reliable skeletal  $q$  can be obtained by using the proposed method.

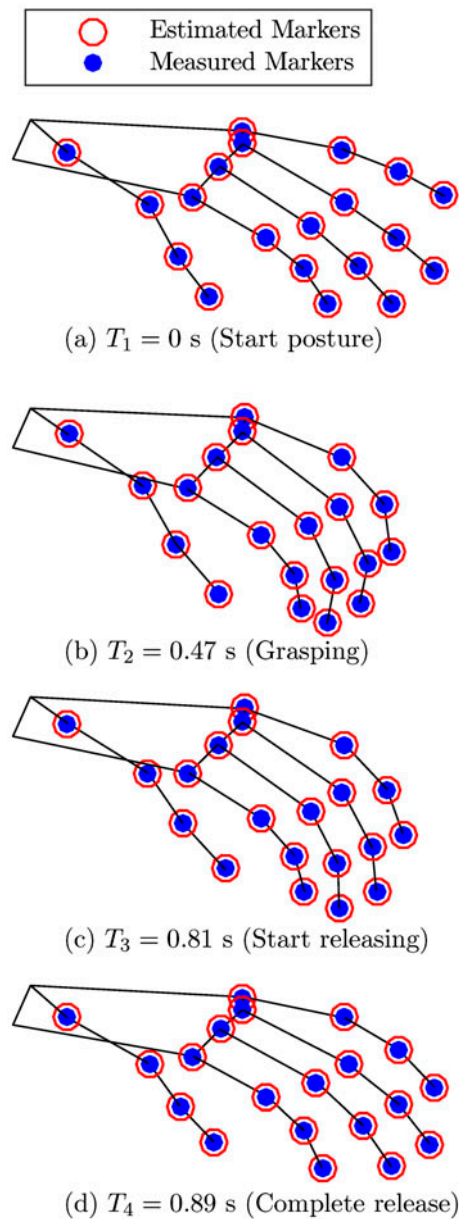


**Figure 11.** Comparison between measured and estimated  $X_i$  in Task D2 for an exemplar subject at different instants (from  $T_1$  to  $T_4$ ).

#### 4. Conclusion

An accurate human hand kinematics model, including the four fingers (4 actuated DoFs each), the thumb (5 actuated DoFs and 1 passive DoF) and the palm arc (4 actuated DoFs), has been proposed along with an identification procedure that estimates joint CoRs. These estimated CoRs are part of the mapping functions between surface and skeleton kinematics. With the identification and validation scheme, the accuracy of sub-millimetre level indicates that the proposed model and associated identification procedure are consistent and highly accurate. The

proposed thumb model with the 5 actuated DoFs and the 1 passive DoF has significantly improved accuracy compared to existing thumb models. Despite the fact that we did not investigate similar passive movements in the other digits, the passive DoFs obviously exist in the other digits. Future work will address: (1) the passive DoFs and their elasticity in all hand joints and (2) the changes of  $d_k$  during tasks with respect to joint DoFs, joint capsule elasticity and physical finger-object interactions. Besides, the identification will be more efficient, when  $\|h_i\|$  can be automatically estimated instead of manual measurement.

#### Notes

1. A passive DoF is a flexible joint that is not actuated by muscles.
2. An actuated or active DoF is a joint that is actuated by muscles.
3. The angular difference is defined as  $\arccos(2\langle\xi_1, \xi_2\rangle^2 - 1)$ , where  $\xi_1$  and  $\xi_2$  denote the quaternions of two rotation matrices, and  $\langle\cdot, \cdot\rangle$  is the inner product.

#### Disclosure statement

We hereby declare that all authors of this paper have no financial or personal relationships with other people or organizations that could inappropriately influence (bias) our work.

#### Funding

Parts of this work are part of a project that has received funding from the European Union's Horizon 2020 research and innovation programme [grant agreement number 688857]. This work is partially funded from the greatly appreciated 'Alfried Krupp Prize for Young University Lecturers'.

#### References

- Braido P, Zhang X. 2004. Quantitative analysis of finger motion coordination in hand manipulative and gestic acts. *Human Mov Sci.* 22:661–678.
- Buchholz B, Armstrong TJ, Goldstein SA. 1992. Anthropometric data for describing the kinematics of the human hand. *Ergonomics.* 35(3):261–273.
- Carpinella I, Mazzoleni P, Rabuffetti M, Thorsen R, Ferrarin M. 2006. Experimental protocol for the kinematic analysis of the hand: definition and repeatability. *Gait Posture.* 23:445–454.
- Cerveri P, Momi ED, Lopomo N, Baud-Bovy G, Barros RML, Ferrigno G. 2007. Finger kinematic modeling and real-time hand motion estimation. *Ann Biomed Eng.* 35(11):1989–2002.
- Cobos S, Ferre M, Sánchez-Urán MA, Ortego J, Aracil R. 2010. Human hand descriptions and gesture recognition for object manipulation. *Comput Methods Biomech Biomed Eng.* 13(3):305–317.
- Cooney WP, Lucca MJ, Chao EYS, Linscheid RL. 1981. The kinesiology of the thumb trapeziometacarpal joint. *J Bone Joint Surg.* 63-A(9):1371–1381.



- Cordella F, Zollo L, Salerno A, Accoto D, Guglielmelli E, Siciliano B. 2014. Human hand motion analysis and synthesis of optimal power grasps for a robotic hand. *Int J Adv Robot Syst.* 11(37):1–13.
- Degeorges R, Parasie J, Mitton D, Imbert N, Goubier J-N, Lavaste F. 2005. Three-dimensional rotations of human three-joint fingers: an optoelectronic measurement. preliminary results. *Surg Radiol Anat.* 27(1):43–50.
- Kapandji AI. 2007. *The physiology of the joints: annotated diagrams of the mechanics of the human joints.* 6th ed. Vol. 1. London: Churchill Livingstone.
- Kuczynski K. 1974. Carpometacarpal joint of the human thumb. *J Anat.* 118:119–126.
- Levangie PK, Norkin CC. 2005. *Joint structure and function: a comprehensive analysis.* 4th ed. Philadelphia (PA): F.A. Davis Co.
- Lippert LS. 2011. *Clinical kinesiology and anatomy.* 5th ed. Philadelphia (PA): F. A. Davis Co.
- Metcalf CD, Notley SV, Chappell PH, Burrige JH, Yule VT. 2008. Validation and application of a computational model for wrist and hand movements using surface markers. *IEEE Trans Biomed Eng.* 55(3):1199–1210.
- Miyata N, Kouchi M, Kurihara T, Mochimaru M. 2004. Modeling of human hand link structure from optical motion capture data. *Proceedings of 2004 IEEE/RSJ International Conference on Intelligent Robots and Systems; Sendai, Japan.* p. 2129–2135.
- Nataraj R, Li Z-M. 2013. Robust identification of three-dimensional thumb and index finger kinematics with a minimal set of markers. *J Biomed Eng.* 135(9):0910021–0910029.
- Nataraj R, Li Z-M. 2015. Integration of marker and force data to compute three-dimensional joint moments of the thumb and index finger jigits during pinch. *Comput Methods Biomech Biomed Eng.* 18(16):592–606.
- Parasuraman S, Zhen CCS. 2009. Development of robot assisted hand stroke rehabilitation system. *International Conference on Computer and Automation Engineering.* Bangkok, Thailand.
- Peña Pitarch E, Falguera NT, Yang JJ. 2014. Virtual human hand: model and kinematics. *Comput Methods Biomech Biomed Eng.* 17(5):568–579.
- Peña Pitarch E, Yang J, Abdel-Malek K. 2005. Santos™ hand: a 25 degree-of-freedom model. *Proc. of SAE Digital Human Modeling for Design and Engineering.* Iowa City, USA.
- Reddy AC. 2014. Difference between Denavit–Hartenberg (D–H) classical and modified conventions for forward kinematics of robots with case study. *International Conference on Advanced Materials and manufacturing Technologies (AMMT); Dec; Chandigarh, India: JNTUH College of Engineering Hyderabad.*
- Shen ZL, Mondello TA, Nataraj R, Domalain MF, Li Z-M. 2012. A digit alignment device for kinematic analysis of the thumb and index finger. *Gai.* 36:643–645.
- Speirs AD, Small CF, Bryant JT, Pichora DR, Zee BY. 2001. Three-dimensional metacarpophalangeal joint kinematics using two markers on the phalanx. *J Eng Med.* 2015(4):415–419.
- Supuk TG, Harwin W, Zanchi V. 2004. Calculating positions of the finger joints centres of rotations in flexion-extension movement from reflective markers. *Proceedings of The IMEKO, IEEE, SICE 2nd International Symposium on Measurement, Analysis and Modeling of Human Functions; Genova, Italy.* p. 363–366.
- Veber M, Bajd T. 2006. Assessment of human hand kinematics. *Proceedings of the 2006 IEEE International Conference on Robotics and Automation; May; Orlando, FL.* p. 2966–2971.
- Veber M, Bajd T, Munih M. 2006. Assessment of finger joint angles and calibration of instrumental glove. *Advances in Robot Kinematics; New York (NY): Springer-Verlag New York Inc.* p. 185–192.
- Zhang X, Lee S-W, Braido P. 2003. Determining finger segmental centers of rotation in flexion-extension based on surface marker measurement. *Journal of Biomechanics.* 36:1097–1102.

## Appendix 1. D–H parameters

**Table A1.** D–H parameters of surface kinematics.

Frame $k$	$\theta_k$	$d_k$	$a_k$	$\alpha_k$	DoF
1st digit					
1	$Q_1$	0	0	$\pi/2$	CMC Ab/Ad
2	$Q_2$	0	$L_{MC}$	$-\pi/2$	CMC F/E
3	$Q_3$	0	0	$\pi/2$	MCP Ab/Ad
4	$Q_4$	0	$L_{PP}$	$-\pi/2$	MCP F/E
5	$Q_5$	0	0	$\pi/2$	IP P/S
6	$Q_6$	0	$L_{DP}$	0	IP F/E
2nd–3rd digits					
1	$Q_1$	0	0	$\pi/2$	MCP Ab/Ad
2	$Q_2$	0	$L_{PP}$	0	MCP F/E
3	$Q_3$	$D_3$	$L_{MP}$	0	PIP F/E
4	$Q_4$	$D_4$	$L_{DP}$	0	DIP F/E
4th–5th digits					
1	$Q_1$	0	0	$\pi/2$	CMC Ab/Ad
2	$Q_2$	0	$L_{MC}$	$-\pi/2$	CMC F/E
3	$Q_3$	0	0	$\pi/2$	MCP Ab/Ad
4	$Q_4$	0	$L_{PP}$	0	MCP F/E
5	$Q_5$	$D_5$	$L_{MP}$	0	PIP F/E
6	$Q_6$	$D_6$	$L_{DP}$	0	DIP F/E

**Table A2.** D–H parameters of skeletal kinematics.

Frame $k$	$\theta_k$	$d_k$	$a_k$	$\alpha_k$	DoF
1st digit					
1	$q_1$	0	0	$\pi/2$	CMC Ab/Ad
2	$q_2$	0	$l_{MC}$	$-\pi/2$	CMC F/E
3	$q_3$	0	0	$\pi/2$	MCP Ab/Ad
4	$q_4$	0	$l_{PP}$	$-\pi/2$	MCP F/E
5	$q_5$	0	0	$\pi/2$	IP P/S
6	$q_6$	0	$l_{DP}$	0	IP F/E
2nd–3rd digits					
1	$q_1$	0	0	$\pi/2$	MCP Ab/Ad
2	$q_2$	0	$l_{PP}$	0	MCP F/E
3	$q_3$	$d_3$	$l_{MP}$	0	PIP F/E
4	$q_4$	$d_4$	$l_{DP}$	0	DIP F/E
4th–5th digits					
1	$q_1$	0	0	$\pi/2$	CMC Ab/Ad
2	$q_2$	0	$l_{MC}$	$-\pi/2$	CMC F/E
3	$q_3$	0	0	$\pi/2$	MCP Ab/Ad
4	$q_4$	0	$l_{PP}$	0	MCP F/E
5	$q_5$	$d_5$	$l_{MP}$	0	PIP F/E
6	$q_6$	$d_6$	$l_{DP}$	0	DIP F/E

## Appendix 2. Solving for rotational angles

$Q$ 's for 1st digit. The 6 DoFs of the thumb are calculated as in (B1a)–(B1f).

$$Q_1 = \text{atan2}({}^0Y_{MCP}, {}^0X_{MCP}), \quad (\text{B1a})$$

$$Q_2 = \text{atan2}\left({}^0Z_{MCP}, \frac{{}^0X_{MCP}}{\cos Q_1}\right), \quad (\text{B1b})$$

$$Q_3 = \text{atan2}({}^2Y_{IP}, {}^2X_{IP}), \quad (\text{B1c})$$

$$Q_4 = \text{atan2}\left({}^2Z_{IP}, \frac{{}^2X_{IP}}{\cos Q_3}\right), \quad (\text{B1d})$$

$$Q_5 = \text{atan2}({}^4Y_{Tip}, {}^4X_{Tip}), \quad (\text{B1e})$$

$$Q_6 = \text{atan2}\left({}^4Z_{Tip}, \frac{{}^4X_{Tip}}{\cos Q_5}\right) \quad (\text{B1f})$$

where

${}^0X_{MCP}$ : is the  $x$ -component of MCP landmark position in  $\{0\}$

${}^0Y_{MCP}$ : is the  $y$ -component of MCP landmark position in  $\{0\}$

${}^0Z_{MCP}$ : is the  $z$ -component of MCP landmark position in  $\{0\}$

${}^2X_{IP}$ : is the  $x$ -component of IP landmark position in  $\{2\}$

${}^2Y_{IP}$ : is the  $y$ -component of IP landmark position in  $\{2\}$

${}^2Z_{IP}$ : is the  $z$ -component of IP landmark position in  $\{2\}$

${}^4X_{Tip}$ : is the  $x$ -component of Tip landmark position in  $\{4\}$

${}^4Y_{Tip}$ : is the  $y$ -component of Tip landmark position in  $\{4\}$

${}^0X_i$  is calculated by (3) and the transformation matrix  ${}^B T_0$ .

${}^k X_i$  is calculated by (3) and the  $Q_{1...k}$  from the previous steps.

$Q$ 's for 2nd–3rd digits. The 4 DoFs are calculated as in (B2a–B2d).

$$Q_1 = \text{atan2}({}^0Y_{PIP}, {}^0X_{PIP}), \quad (\text{B2a})$$

$$Q_2 = \text{atan2}\left({}^0Z_{PIP}, \frac{{}^0X_{PIP}}{\cos Q_1}\right), \quad (\text{B2b})$$

$$Q_3 = \text{atan2}({}^2Y_{DIP}, {}^2X_{DIP}), \quad (\text{B2c})$$

$$Q_4 = \text{atan2}({}^3Y_{Tip}, {}^3X_{Tip}) \quad (\text{B2d})$$

where

${}^0X_{PIP}$ : is the  $x$ -component of PIP landmark position in  $\{0\}$

${}^0Y_{PIP}$ : is the  $y$ -component of PIP landmark position in  $\{0\}$

${}^0Z_{PIP}$ : is the  $z$ -component of PIP landmark position in  $\{0\}$

${}^2X_{DIP}$ : is the  $x$ -component of DIP landmark position in  $\{2\}$

${}^2Y_{DIP}$ : is the  $y$ -component of DIP landmark position in  $\{2\}$

${}^3X_{Tip}$ : is the  $x$ -component of Tip landmark position in  $\{3\}$

${}^3Y_{Tip}$ : is the  $y$ -component of Tip landmark position in  $\{3\}$

${}^0X_i$  is calculated by (3) and the transformation matrix  ${}^B T_0$ .

${}^k X_i$  is calculated by (3) and the  $Q_{1...k}$  from the previous steps.

$Q$ 's for 4th–5th digits. Equations (B3a)–(B3f) are used to calculate the rotational angles as follows:

$$Q_1 = \text{atan2}({}^B Y_{MCP}, {}^B X_{MCP}), \quad (\text{B3a})$$

$$Q_2 = \text{atan2}\left({}^B Z_{MCP}, \frac{{}^B X_{MCP}}{\cos Q_1}\right), \quad (\text{B3b})$$

$$Q_3 = \text{atan2}({}^2Y_{PIP}, {}^2X_{PIP}), \quad (\text{B3c})$$

$$Q_4 = \text{atan2}\left({}^2Z_{PIP}, \frac{{}^2X_{PIP}}{\cos Q_3}\right), \quad (\text{B3d})$$

$$Q_5 = \text{atan2}({}^4Y_{DIP}, {}^4X_{DIP}), \quad (\text{B3e})$$

$$Q_6 = \text{atan2}({}^5Y_{Tip}, {}^5X_{Tip}) \quad (\text{B3f})$$

where

${}^B X_{MCP}$ : is the  $x$ -component of MCP landmark position in  $\{B\}$

${}^B Y_{MCP}$ : is the  $y$ -component of MCP landmark position in  $\{B\}$

${}^B Z_{MCP}$ : is the  $z$ -component of MCP landmark position in  $\{B\}$

${}^2X_{PIP}$ : is the  $x$ -component of PIP landmark position in  $\{2\}$

${}^2Y_{PIP}$ : is the  $y$ -component of PIP landmark position in  $\{2\}$

${}^2Z_{PIP}$ : is the  $z$ -component of PIP landmark position in  $\{2\}$

${}^4X_{DIP}$ : is the  $x$ -component of DIP landmark position in  $\{4\}$

${}^4Y_{DIP}$ : is the  $y$ -component of DIP landmark position in  $\{4\}$

${}^5X_{Tip}$ : is the  $x$ -component of Tip landmark position in  $\{5\}$

${}^5Y_{Tip}$ : is the  $y$ -component of Tip landmark position in  $\{5\}$

${}^k X_i$  is calculated by (3) and the  $Q_{1...k}$  from the previous steps.

### Appendix 3. Estimation of $h_i$

The calculations of the vector  $h_i$  are detailed in this section for different joints of the 2nd to 5th digits. Considering the difference in defining the joint F/E plane in the thumb joints, the vector  $h_i$  is estimated analogous to the other fingers. Figure 2 shows the finger 2-D F/E plane and parameters definition to calculate  $h_i$ . the vector  $h_i$  for joints of 2nd–5th digits is calculated as follows.

*DIP joint.* The vector  $h_{DIP}$  is defined as

$$h_{DIP} = \|h_{DIP}\| e_{h_{DIP}}. \quad (\text{C1})$$

The unit vector  $e_{h_{DIP}}$  can be obtained as in Supuk et al. (2004) from

$$\mathbf{L}_{DP} \cdot \mathbf{e}_{h_{DIP}} = \|\mathbf{L}_{DP}\| \|\mathbf{e}_{h_{DIP}}\| \cos \alpha_{DIP}, \quad (C2a)$$

$$-\mathbf{L}_{MP} \cdot \mathbf{e}_{h_{DIP}} = \|\mathbf{L}_{MP}\| \|\mathbf{e}_{h_{DIP}}\| \cos \beta_{DIP}, \quad (C2b)$$

as

$$\mathbf{e}_{h_{DIP}} = \begin{pmatrix} \mathbf{L}_{DP}^T \\ -\mathbf{L}_{MP}^T \end{pmatrix}^{-1} \begin{pmatrix} \|\mathbf{L}_{DP}\| \cos \alpha_{DIP} \\ \|\mathbf{L}_{MP}\| \cos \beta_{DIP} \end{pmatrix}, \quad (C3)$$

where  $\alpha_{DIP}$  is obtained from the Law of Cosines as

$$\alpha_{DIP} = \arccos \frac{\|\mathbf{L}_{DP}\|^2 - \|\mathbf{L}_{MP}\|^2 - \|\mathbf{h}_{DIP}\|^2}{-2\|\mathbf{L}_{DP}\| \|\mathbf{h}_{DIP}\|} \quad (C4)$$

and  $\beta_{DIP}$  from

$$\beta_{DIP} = \pi - (Q_4 + \alpha_{DIP}) \quad (C5)$$

*PIP joint.* Analogous to C1, the vector  $\mathbf{h}_{PIP}$  is defined as

$$\mathbf{h}_{PIP} = \|\mathbf{h}_{PIP}\| \mathbf{e}_{h_{PIP}}, \quad (C6)$$

with the unit vector  $\mathbf{e}_{h_{PIP}}$  being found by solving

$$\mathbf{e}_{h_{PIP}} = \begin{pmatrix} \mathbf{L}_{MP}^T \\ -\mathbf{L}_{PP}^T \end{pmatrix}^{-1} \begin{pmatrix} \|\mathbf{L}_{MP}\| \cos \alpha_{PIP} \\ \|\mathbf{L}_{PP}\| \cos \beta_{PIP} \end{pmatrix}. \quad (C7)$$

The angle  $\alpha_{PIP}$  is defined as

$$\begin{aligned} \alpha_{PIP} &= \alpha'_{PIP} + \alpha''_{PIP} \\ \alpha'_{PIP} &= \arccos \frac{\|\mathbf{h}_{DIP}\|^2 - \|\mathbf{L}_{MP}\|^2 - \|\mathbf{d}_{MP}\|^2}{-2\|\mathbf{L}_{MP}\| \|\mathbf{d}_{MP}\|} \\ \alpha''_{PIP} &= \arccos \frac{\|\mathbf{L}_{MP}\|^2 - \|\mathbf{h}_{PIP}\|^2 - \|\mathbf{d}_{MP}\|^2}{-2\|\mathbf{h}_{PIP}\| \|\mathbf{d}_{MP}\|} \end{aligned} \quad (C8)$$

and  $\beta_{PIP}$  is

$$\beta_{PIP} = \pi - (Q_3 + \alpha_{PIP}). \quad (C9)$$

*MCP joint.* The vector  $\mathbf{h}_{MCP}$  is defined analogous to (C1), where the unit vector  $\mathbf{e}_{h_{MCP}}$  is calculated as

$$\mathbf{e}_{h_{MCP}} = \begin{pmatrix} \mathbf{L}_{PP}^T \\ \mathbf{d}_{PP}^T \end{pmatrix}^{-1} \begin{pmatrix} \|\mathbf{L}_{PP}\| \cos (\alpha'_{MCP} + \alpha''_{MCP}) \\ \|\mathbf{d}_{PP}\| \cos \alpha''_{MCP} \end{pmatrix}, \quad (C10)$$

where  $\alpha'_{MCP}$  and  $\alpha''_{MCP}$  are calculated via the Law of Cosines similar to (C8).



## Appendix 4. Identification algorithms

### Algorithm 1 Identification of ${}^{\text{BH}}\mathbf{R}_{\text{BT}}$

1: <b>Input:</b> $\{{}^{\text{W}}X_i\}$	▷ in Task S1 (Figure 5)
2: <b>Output:</b> ${}^{\text{BH}}\mathbf{R}_{\text{BT}}$	▷ Equation (2)
3: <b>Procedure:</b>	
4: $e_x := \frac{{}^{\text{W}}X_{\text{BHx}} - {}^{\text{W}}X_{\text{BH0}}}{\ {}^{\text{W}}X_{\text{BHx}} - {}^{\text{W}}X_{\text{BH0}}\ };$	▷ establish {BH}, $x$ -axis
5: $e_y := \frac{{}^{\text{W}}X_{\text{BHy}} - {}^{\text{W}}X_{\text{BH0}}}{\ {}^{\text{W}}X_{\text{BHy}} - {}^{\text{W}}X_{\text{BH0}}\ };$	▷ $y$ -axis
6: $e_z := e_x \times e_y;$	▷ $z$ -axis (right-hand rule)
7: ${}^{\text{W}}\mathbf{R}_{\text{BH}} := (e_x \ e_y \ e_z);$	▷ establish ${}^{\text{W}}\mathbf{R}_{\text{BH}}$
8: $\begin{pmatrix} {}^{\text{BH}}X_i \\ 1 \end{pmatrix} := \begin{pmatrix} {}^{\text{W}}\mathbf{R}_{\text{BH}} & {}^{\text{W}}X_{\text{BH0}} \\ \mathbf{0}^T & 1 \end{pmatrix}^{-1} \begin{pmatrix} {}^{\text{W}}X_i \\ 1 \end{pmatrix};$	▷ express positions in {BH}
9: $e_x := \frac{{}^{\text{BH}}X_{\text{BTx}} - {}^{\text{BH}}X_{\text{BT0}}}{\ {}^{\text{BH}}X_{\text{BTx}} - {}^{\text{BH}}X_{\text{BT0}}\ };$	▷ establish {BT}, $x$ -axis
10: $e_y := \frac{{}^{\text{BH}}X_{\text{BTy}} - {}^{\text{BH}}X_{\text{BT0}}}{\ {}^{\text{BH}}X_{\text{BTy}} - {}^{\text{BH}}X_{\text{BT0}}\ };$	▷ $y$ -axis
11: $e_z := e_x \times e_y;$	▷ $z$ -axis (right-hand rule)
12: ${}^{\text{BH}}\mathbf{R}_{\text{BT}} := (e_x \ e_y \ e_z);$	▷ establish ${}^{\text{BH}}\mathbf{R}_{\text{BT}}$

### Algorithm 2 Identification of hand kinematics

1: <b>Inputs:</b> $\{{}^{\text{BH}}X_i\}, \{\ h_i\ \}, HL, {}^{\text{BH}}\mathbf{R}_{\text{BT}}$	▷ $HL$ : hand length
2: <b>Output:</b> $q$	
3: <b>Procedure:</b>	
4: $L_{\text{PP}} := {}^{\text{BH}}X_{\text{MCP}} - {}^{\text{BH}}X_{\text{PIP}};$	
5: $L_{\text{MP}} := {}^{\text{BH}}X_{\text{PIP}} - {}^{\text{BH}}X_{\text{DIP}};$	
6: $L_{\text{DP}} := {}^{\text{BH}}X_{\text{DIP}} - {}^{\text{BH}}X_{\text{Tip}};$	
7: $Q := f^{-1}(X);$	▷ surface kinematics (Section 2.2.1)
8: $\{l_{\square}\} := \text{anthropometric\_model}(HL);$	▷ anthropometric model (Buchholz et al. 1992)
9: $\{h_i\} := h\_estimation(Q, \{L_{\square}\}, \{l_{\square}\}, \{\ h_i\ \});$	▷ estimation of $h_i$ (Appendix 3)
10: $x_i := X_i - h_i;$	
11: $q := g^{-1}(x);$	▷ skeletal kinematics (Section 2.2.1)